Research in Astronomy and Astrophysics, 25:055015 (9pp), 2025 May
https://doi.org/10.1088/1674-4527/adce8e
CSTR: 32081.14.RAA.adce8e

The Nature of the Accretion Physics in Quiescent Black Hole System LB-1

Tong Su[1,2,3], Erlin Qiao[1,2], Song Wang[1,4], and Qi Guo[1,2,3]
[1] National Astronomical Observatories, Chinese Academy of Sciences, Beijing 100101, China; sutong@bao.ac.cn
[2] School of Astronomy and Space Science, University of Chinese Academy of Sciences, Beijing 100049, China
[3] Key Laboratory for Computational Astrophysics, National Astronomical Observatories, Chinese Academy of Sciences, Beijing 100101, China
[4] Institute for Frontiers in Astronomy and Astrophysics, Beijing Normal University, Beijing 102206, China
Received 2025 March 18; revised 2025 April 10; accepted 2025 April 16; published 2025 May 19

Abstract

LB-1 is a binary system that has drawn great attention since its discovery in 2019. The two components of LB-1 are suggested to be a B-type star plus a black hole (BH). In this paper, we first calculate the wind mass-loss rate of the B-type star. We then calculate the mass capture rate by the BH, with which as the initial mass accretion rate, we calculate the truncation radius of the accretion disk and the corresponding emergent spectra of the accretion flow (comprising an inner advection-dominated accretion flow (ADAF) + an outer truncated accretion disk) within the framework of the disk evaporation model. It is found that the predicted truncation radius of the accretion disk with appropriate model parameters is consistent with observations inferred from the observed broad H_α emission line. The predicted X-ray luminosity is definitely below the estimated upper limits with the sensitivity of the Chandra X-ray Observatory of the X-ray luminosity $\approx 2 \times 10^{31}$ erg s^{-1}, which is also consistent with observations. Finally, we argue that the disk evaporation model can indeed reflect the intrinsic physics of the accretion flow in LB-1, and has potential to be applied to other quiescent BHs in the future.

Key words: accretion, accretion disks – stars: black holes – (stars:) binaries: general – X-rays: binaries

1. Introduction

LB-1 (LS V+22 25) is discovered as a binary system by a radial-velocity monitoring campaign of the Large Aperture Multi-Object Spectroscopic Telescope (LAMOST) in the Kepler K2-0 field of the sky (Liu et al. 2019). The coordinates of LB-1 are (l, b) = (188.°23526, +02.°05089), where l is Galactic longitude and b is Galactic latitude. Besides the stellar absorption lines, a broad H_α emission line is identified in LAMOST spectra, which is almost stationary. Subsequent observations by GTC/OSISRIS and Keck/HIRES confirmed the apparent periodic motion of the stellar absorption lines and the presence of the prominent broad H_α emission line. Meanwhile, it is found that the H_α emission line is moving in an anti-phase with a much smaller amplitude compared with that of the stellar absorption lines. The orbital period of LB-1 is $P = 78.9 \pm 0.3$ days. The semi-amplitude velocities of the stellar absorption line and the H_α emission line are $K_B = 52.8 \pm 0.7\,\mathrm{km\,s^{-1}}$ and $K_A = 6.4 \pm 0.8\,\mathrm{km\,s^{-1}}$, respectively. Spectral modeling with TLUSTY indicates that LB-1 is a B-type main sequence star with a mass of $M_B = 8.2^{+0.9}_{-1.2}\,M_\odot$, an effective temperature $T_{\rm eff} = 18100 \pm 820$ K, and a surface gravity $\log g = 3.43 \pm 0.15$. The dark companion of LB-1 is suggested to be a black hole (BH) (with a minimum mass of $6.3^{+0.4}_{-1.0} M_\odot$) from the mass function measurements, assuming an edge-on orbit. One of the very interesting features of LB-1 is the observed broad H_α emission line with the full width at half-maximum (FWHM) $\approx 240\,\mathrm{km\,s^{-1}}$, which is too broad to be from an interloper M dwarf, surrounding nebulae or a circumbinary disk. It is suggested that the broad H_α emission line is from an accretion disk around the BH, which can consequently be used to trace the motion of the BH. According to the conservation of angular momentum, the mass of the BH can be calculated as $M_{\rm BH} = (K_B/K_A) M_B \approx 68^{+11}_{-13}\,M_\odot$, which corresponds to an inclination angle of 15°–18° if the BH mass is measured with the method of mass function measurement. The derived small inclination angle is consistent with the wine bottle shape of the H_α emission line (Liu et al. 2019).

The estimated BH mass of $M_{\rm BH} \approx 68 M_\odot$ is questioned by some other groups (e.g., Abdul-Masih et al. 2020; Irrgang et al. 2020; Shenar et al. 2020; Simón-Díaz et al. 2020; Yungelson et al. 2020). The debates on the BH mass are mainly from two aspects: (1) whether the H_α emission line can trace the motion of the BH (or even not a BH), (2) the uncertainty for the mass measurements of the B-type star. For example, based on the optical spectra observed by the HERMES spectrograph (Raskin et al. 2011), Abdul-Masih et al. (2020) argue that the observed radial-velocity measurements result from the superposition of the stellar absorption line and a nearly static H_α emission line, so the H_α emission line cannot be used to trace the motion of the BH. In addition, it is argued that the mass of the B-type star is estimated to be $M_B = 4.2^{+0.8}_{-0.7}\,M_\odot$ by fitting the HERMES optical spectra with a local thermodynamic equilibrium (LTE)

atmospheric model (Tkachenko 2015; El-Badry & Quataert 2020). The study in Abdul-Masih et al. (2020) may alleviate the challenge of the presence of a very massive BH at solar metallicity. Further, it is proposed that the companion is a fast-rotating B-type star with a mass similar to that of the primary B-type star. Alternatively, the companion is still possible to be a BH, however, the mass of the BH is suggested to be not greater than $\approx 50\,M_{\odot}$. In Simón-Díaz et al. (2020), the authors propose that the B-type star is a slightly evolved main sequence star with a mass of $\approx$3–5 $M_{\odot}$ by jointly fitting the spectra of TNG/HARPS-N, GTC/HORuS, and Keck/HIRES used in Liu et al. (2019) with the non-LTE stellar atmosphere code FASTWIND. The mass of the BH is derived to be $\approx$4–5 $M_{\odot}$ by assuming an edge-on orbit with the method of mass function measurement. In Irrgang et al. (2020), the authors reanalyze the Keck/HIRES spectra used in Liu et al. (2019) with a different stellar atmosphere model (Irrgang et al. 2014, 2018), and find that the B-type spectral star of LB-1 is a stripped helium star with a mass of $M_{\rm B} = 1.1 \pm 0.5 M_{\odot}$ rather than a B-type main sequence star. Further, the authors suggest that the dark companion of LB-1 is a compact object with a minimum mass of 2–3 $M_{\odot}$ based on the mass function measurement, which could be a mass gap BH, a massive neutron star, or even a main sequence star. Combining the observed spectral data of HERMES and FEROS spectrographs, Shenar et al. (2020) also suggest that the primary of LB-1 is a stripped helium star with a mass of $\approx 1\,M_{\odot}$. Meanwhile, it is suggested that the dark companion is a Be star, which contributes about 45% optical flux. Assuming a typical value of $7 \pm 2\,M_{\odot}$ for the Be star (i.e., the dark companion), the mass of the primary of LB-1 is further constrained to be a mass of $1.5 \pm 0.4\,M_{\odot}$, and the orbital inclination angle of LB-1 is estimated to be $39^{\circ} \pm 4^{\circ}$.

In order to respond to the debates on the mass of the dark companion, Liu et al. (2020) conduct a new study, analyzing the Paβ and Paγ emission lines observed with Calar Alto high-resolution search for M dwarfs with Exo-earths with Near-infrared and optical Echelle Spectrographs (CARMENES) mounted on the 3.5 m telescope at the Calar Alto Observatory. The phase-averaged Paβ and Paγ emission lines show a cleaner, double-peaked disk-like profile, which is clearer for exploring the properties of the dark companion compared with the H_{α} emission line due to the complex distortion of H_{α} emission line. The authors measured the shift of the line center of the Paβ and Paγ emission lines, showing a perfect anti-phase motion with the stellar absorption lines. The semi-amplitude velocity of the Paβ and Paγ emission lines is in the range of 8–13 km s^{-1}. Further, based on the line profile, it is proved that the Paβ and Paγ emission lines can trace the dark companion, ruling out the circumbinary disk and the hierarchical triple cases. Combining the semi-amplitude of the stellar absorption line for the primary B-type star and the Paβ and Paγ emission lines for the dark companion, the inferred mass ratio of the dark companion to the primary B-type star is 5.1 ± 0.8. Finally, several possibilities for the nature of the two components of LB-1, in particular, a B-type main sequence star plus a BH (B+BH), a stripped helium star plus a Be star ($B_{\rm He}$+Be) are discussed (Liu et al. 2020).

Recently, Lennon et al. (2021) tested the scenarios of B+BH and $B_{\rm He}$+Be by fitting the UV-optical spectra obtained from the Space Telescope Imaging Spectrograph (STIS) and the IR spectra obtained from Wide Field Camera 3 (WFC3) onboard the Hubble Space Telescope (HST). It shows that the B+BH model is preferred, particularly for explaining the UV spectrum. In the B+BH scenario, the mass of the B-type star is fitted to be $5.1^{+1.8}_{-1.4}\,M_{\odot}$, and the mass of the BH is derived to be $21^{+9}_{-8}\,M_{\odot}$ by assuming a mass ratio of the dark companion to the primary 5.1 ± 0.1 as suggested in Liu et al. (2020).

In this paper, we investigate the properties of the accretion flow with the scenario of B+BH for LB-1. Specifically, we calculate the wind mass-loss rate of the B-type star and the mass rate captured by the BH. Using this as the initial mass accretion rate, we calculate the truncation radius of the accretion disk and the corresponding emergent spectra of the accretion flow (comprising an inner advection-dominated accretion flow (ADAF) + an outer truncated accretion disk) within the framework of the disk evaporation model. The generally predicted features by the disk evaporation model of the accretion flow, such as the truncation radius of the accretion disk, the very dim X-ray emission (non-detection), as well as the nearly neglected UV-optical emission compared to that of the B-type star, are consistent with observations of LB-1. Finally, we discuss the effect of the viscosity parameter α on the multi-band emission of the accretion flow. In Section 2, we calculate the wind mass-loss rate of the B-type star and the mass rate captured by the BH in LB-1. In Section 3, we briefly introduce the disk evaporation model and the corresponding predicted features as applied in LB-1. The discussions are presented in Section 4, and the conclusions are drawn in Section 5.

2. The Models

2.1. Wind Mass-loss Rate of the B-type Star and the Mass Rate Captured by the BH

We first calculate the wind mass-loss rate of the B-type star, following (Vink et al. 2000),

$$\begin{aligned}\log \dot{M}_{\rm win} = & -6.688 + 2.21 \log (L_{\rm B}/10^5) \\ & - 1.339 \log (M_{\rm B}/30) \\ & - 1.601 \log \left(\frac{v_{\infty}/v_{\rm esc}}{2.0} \right) \\ & + 1.07 \log (T_{\rm eff}/20000), \end{aligned} \quad (1)$$

where $\dot{M}_{\rm win}$ is the wind mass-loss rate in units of $M_{\odot}\,{\rm yr}^{-1}$, $L_{\rm B}$ and $M_{\rm B}$ are the bolometric luminosity and the mass of the B-type star respectively in solar units, $T_{\rm eff}$ is the effective

Table 1
System Parameters of LB-1, Taken from Liu et al. (2019) (G1) and Lennon et al. (2021) (G2), Respectively

System Parameter	L_B ($L_\odot$) (1)	M_B ($M_\odot$) (2)	R_B ($R_\odot$) (3)	T_{eff} (K) (4)	$\log g$ (5)	K_B (km s^{-1}) (6)	P (days) (7)	$\sin i$ (8)	M_{BH} ($M_\odot$) (9)
G1	7000	8.2	9.0	18000	3.43	52.8	78.9	0.28	68
G2	1698	5.2	6.0	15300	3.6	52.6	78.9	0.43	21

Note. L_B, M_B, R_B, T_{eff}, $\log g$, and K_B are the luminosity, mass, radius, effective temperature, logarithm of the surface gravity, and the semi-amplitude velocity of the B-type star, and M_{BH} is the BH mass, all scaled to solar units.

temperature at the surface of the B-type star, and v_∞/v_{esc} is the ratio of the terminal velocity v_∞ to the effective escape velocity at the stellar surface v_{esc} of the wind, $v_{esc} = \sqrt{\frac{2GM_B(1-\Gamma_e)}{R_B}}$, where G is the gravitational constant, R_B is the radius of the B-type star, and $\Gamma_e \equiv L_B/L_{Edd} = \kappa_e L_B/(4\pi cGM_B)$ is the Eddington parameter. Equation (1) is valid for T_{eff} in the range of 12,500 K $< T_{eff} <$ 22,500 K; in this temperature range $v_\infty/v_{esc} = 1.3$. The wind velocity near the BH v_{win} can be expressed as,

$$v_{win}(A) = v_\infty\left(1 - \frac{R_B}{A}\right)^\beta, \quad (2)$$

where A is the separation of the binary system, calculated as $A = \left[\frac{G(M_B+M_{BH})P^2}{4\pi^2}\right]^{1/3}$ with Kepler's third law. M_{BH} is the mass of the BH, and P is the orbital period. The index β is $\approx$1 for OB supergiants (Vink et al. 2000).

The mass capture radius can be estimated in terms of the Bondi-Hoyle prescription (See Section 4.9 in Frank et al. 2002),

$$R_{cap} = \frac{2GM_{BH}}{v_{win}^2}, \quad (3)$$

and the mass rate captured by the BH, $\dot{M}_{cap}$, can then be expressed as,

$$\dot{M}_{cap} = \frac{\pi R_{cap}^2}{4\pi A^2}\dot{M}_{win}. \quad (4)$$

Combining Equations (1), (2), (3), and (4), we calculate $\dot{M}_{cap}$ by specifying L_B, M_B, R_B, T_{eff}, $M_{BH,}$ and P measured in LB-1. In this paper, two groups of system parameters of LB-1, named G1 and G2, are used for calculating $\dot{M}_{cap}$. One can refer to Table 1 for the data of G1 and G2 for details. The data of G1 are from Liu et al. (2019), which is the original paper for LB-1, and the data of G2 are from Lennon et al. (2021) (note that the period P and the semi-amplitude K_B are taken from Liu et al. 2020), in which by fitting the UV-optical spectra obtained from STIS and the IR spectrum spectra obtained from WFC3 onboard HST, the authors find that the fitting results of the B+BH model are more preferred than those of the B_{He}+Be model for LB-1. We list the value of $\dot{M}_{cap}$ in column (6) of Table 2, in which $\dot{M}_{cap}$ is $3.08 \times 10^{-11}\,M_\odot\,yr^{-1}$ for G1 and $4.32 \times 10^{-13}\,M_\odot\,yr^{-1}$ for G2. The mass rate captured by the BH $\dot{M}_{cap}$, can be regarded as the initial mass accretion rate fed to the BH, denoted as $\dot{M}$ hereafter. One may note that in this paper, we adopt the wind-fed scenario to calculate the BH accretion rate rather than the Roche-Lobe overflow scenario. This is because the LB-1 system has a long orbital period, and the large separation between the B-type star and the BH prevents the Roche-Lobe mass transfer. We calculate the distance from the center of the B-type star to the inner Lagrange point L_1 of the binary system b_1 as $b_1 = (0.5 - 0.227\log(M_{BH}/M_B))A$ (See page 54 in Frank et al. 2002). We show that b_1 is always greater than the radius of the B-type star, which supports the wind-fed scenario for the calculation of the BH accretion rate. [5]

In this paper, we define a dimensionless mass accretion rate, i.e., $\dot{m} \equiv \dot{M}/\dot{M}_{Edd}$ (with $\dot{M}_{Edd} = L_{Edd}/0.1c^2 = 1.39 \times 10^{18} M_{BH}/M_\odot$ g s^{-1}) for convenience. We list $\dot{m}$ in column (7) of Table 2. The value of $\dot{m}$ is 2.05×10^{-5} for G1 and 9.32×10^{-7} for G2. We also list the value of the separation of the binary system A, the capture radius R_{cap}, the wind mass-loss rate of the B-type star $\dot{M}_{win}$, and sin i of the binary system (with i being the inclination angle of the orbit of the binary system), which can be found in Table 2 for details.

2.2. A Summary of the Disk Evaporation Model

With the mass accretion rate $\dot{m}$ calculated in Section 2.1, we further investigate the geometry of the accretion flow and the corresponding emergent spectra. We assume that the accretion flow is in the form of the standard accretion disk initially (Shakura & Sunyaev 1973), since strong evidence indicates the presence of an accretion disk around the BH as inferred from modeling the profiles of H_α (Liu et al. 2019), Paβ, and Paγ emission lines (Liu et al. 2020). In general, there exists a

[5] For our G1 data, where $M_B = 8.2M_\odot$, $M_{BH} = 68M_\odot$, $A = 2.28 \times 10^{13}$ cm, b_1 is calculated to be 6.65×10^{12} cm, which is 10 times larger than the radius of the B-type star with $R_B = 9R_\odot = 6.3 \times 10^{11}$ cm. For our G2 data, where $M_B = 5.2M_\odot$, $M_{BH} = 21M_\odot$, $A = 1.6 \times 10^{13}$ cm, b_1 is calculated to be 5.79×10^{12} cm, which is also more than 10 times larger than the radius of the B-type star with $R_B = 6R_\odot = 4.2 \times 10^{11}$ cm.

Table 2
Derived Parameters of LB-1

Derived Parameter	A (10^{13} cm) (1)	A ($10^6 R_S$) (2)	R_{cap} (10^{12} cm) (3)	R_{cap} ($10^5 R_S$) (4)	$\dot{M}_{win}$ ($M_\odot$ yr^{-1}) (5)	$\dot{M}_{cap}$ ($M_\odot$ yr^{-1}) (6)	$\dot{m}$ ($\dot{m} \equiv \dot{M}/\dot{M}_{Edd}$) (7)	$\sin i$ (8)
G1	2.28	1.14	3.32	1.66	5.81×10^{-9}	3.08×10^{-11}	2.05×10^{-5}	0.28
G2	1.60	2.58	1.06	1.71	3.93×10^{-10}	4.32×10^{-13}	9.32×10^{-7}	0.43

Note. Columns (1) and (2) are the separation of the binary system A, in units of cm and R_S, respectively. Columns (3) and (4) are the capture radius R_{cap}, in units of cm and R_S respectively. Column (5) is the wind mass-loss rate of the B-type star, $\dot{M}_{win}$, in units of $M_\odot$ yr^{-1}, and Column (6) is the mass rate captured by the BH, $\dot{M}_{cap}$, in units of $M_\odot$ yr^{-1}. Column (7) is the mass accretion rate fed to the BH in units of $\dot{M}_{Edd}$. Column (8) is sin$i$ of the binary system with i being the inclination angle of the orbit.

critical mass accretion rate $\dot{m}_{crit}$ (accretion rate in units of $\dot{M}_{Edd}$). If $\dot{m}$ is greater than $\dot{m}_{crit}$, the standard accretion disk will extend down to the innermost stable circular orbit (ISCO) of the BH. While if $\dot{m}$ is less than $\dot{m}_{crit}$, the accretion disk will truncate at some radius. The truncation radius generally decreases with increasing mass accretion rate. Several models have been proposed for $\dot{m}_{crit}$ and the truncation radius of the accretion disk. One of the most promising models for $\dot{m}_{crit}$ and the truncation of the accretion disk is the disk evaporation model (Meyer & Meyer-Hofmeister 1994; Liu et al. 1999; Meyer et al. 2000a, 2000b; Liu et al. 2002a; Qiao & Liu 2009, 2010; Taam et al. 2012). In Taam et al. (2012), the authors summarized the main results of the disk evaporation model, giving general formulae for $\dot{m}_{crit}$ and the truncation radius of the accretion disk. We list $\dot{m}_{crit}$ and the truncation radius r_{tr} as follows,

$$\dot{m}_{crit} \approx 0.38\alpha^{2.34}\beta^{-0.41}, \quad (5)$$

$$r_{tr} \approx 17.3\dot{m}^{-0.886}\alpha^{0.07}\beta^{4.61}, \quad (6)$$

where α is the viscosity parameter, β is the magnetic parameter (with magnetic pressure $p_m = B^2/8\pi = (1-\beta)p_{tot}$, $p_{tot} = p_{gas} + p_m$). r_{tr} is the truncation radius in units of Schwarzschild radius R_S (with $R_S = 2GM_{BH}/c^2 \approx 2.95 \times 10^5 M_{BH}/M_\odot$ cm) [6].

3. Results

3.1. The Truncation Radius of the Accretion Disk

According to Equation (6), the truncation radius of the accretion disk r_{tr} can be calculated by specifying $\dot{m}$, α, and β. It can be seen from Equation (6) that r_{tr} is very weakly dependent on α. Initially, we fix $\alpha = 0.3$ as adopted in several literatures for the quiescent BH X-ray binaries (e.g., Yuan et al. 2005; Zhang et al. 2010). Meanwhile, the effect of β on r_{tr} is very strong as discussed in Meyer & Meyer-Hofmeister (2002), Qian et al. (2007), and Taam et al. (2012). We test the effect of β on r_{tr} for a given value of $\dot{m}$ derived from the system parameters G1 and G2 of LB-,1, respectively.

For the system parameter G1, $\dot{m}$ is calculated to be 2.05×10^{-5}. Substituting $\dot{m}$ into Equation (6), r_{tr} are calculated to be 8.10×10^4, 6.01×10,^{4} and $4.37 \times 10^4 R_S$ for $\beta = 0.8$, 0.75, and 0.7,0, respectively. Assuming that the truncated accretion disk is Keplerian in the angular direction, at r_{tr} the projected velocity in the line of sight can be calculated as $v_{K,tr}\sin i$, which are $\approx$ 209.57, 243.18, 285.10 km s^{-1} for $\beta = 0.8$, 0.75, and 0.70, respectively. We further calculate the effective temperature at the surface of the accretion disk $T_{eff}(r_{tr})$ (Shakura & Sunyaev 1973; Frank et al. 2002), which are $\approx$ 303.72, 379.55, and 481.66 K, respectively. Hydrogen in this temperature range is neutral, which ensures the production of the hydrogen emission line. As for the system parameter G2, $\dot{m}$ is calculated to be 9.32×10^{-7}. In this case, r_{tr} are calculated to be 2.23×10^5, 1.43×10^5, and $8.82 \times 10^4 R_S$ for $\beta = 0.55$, 0.5, and 0.45, respectively. Likewise, assuming that the angular velocity of the truncated accretion disk is the Keplerian velocity, at r_{tr}, $v_{K,tr}\sin i$ are $\approx$194.56, 242.37, 308.99 km s^{-1} for $\beta = 0.55$, 0.5, and 0.45 respectively, and the corresponding $T_{eff}(r_{tr})$ are $\approx$88.17, 122.56, and 176.37 K respectively. For clarity, one can refer to Table 3 for the information related to the truncated radius of the accretion disk.

Clearly, with $\dot{m} = 2.05 \times 10^{-5}$ (based on G1 data) and $\beta = 0.75$, or $\dot{m} = 9.32 \times 10^{-7}$ (based on G2 data) and $\beta = 0.5$, the predicted projected velocity of the truncated disk in the line of sight matches very well with the observed FWHM of the H_α emission line of $\approx$240km s^{-1}. To more easily compare with observations, in Section 3.2, we calculate the corresponding emergent spectra of the accretion flow with $m = 68$, $\dot{m} = 2.05 \times 10^{-5}$, $\alpha = 0.3$ and $\beta = 0.75$, as well as $m = 21$, $\dot{m} = 9.32 \times 10^{-7}$, $\alpha = 0.3$ and $\beta = 0.5$, respectively.

3.2. The Emergent Spectra

Under the framework of the disk evaporation model, inside the truncation radius of the accretion disk, the accretion flow will be in the form of an advection-dominated accretion flow (ADAF). In this case, the geometry of the accretion flow will be an inner ADAF + an outer truncated accretion disk. In this paper, we calculate the emergent spectrum of the accretion flow

[6] Note that the derived formulae for $\dot{m}_{crit}$ and r_{tr} are independent of the black hole mass, so can be applied to both stellar-mass BH and supermassive BH.

Table 3
Parameters of the Accretion Flow

Parameters of the Accretion Flow	$\dot{m}$	α	β	$r_{\rm tr}$ ($R_{\rm S}$)	$v_{\rm K,tr}\sin i$ (km s^{-1})	$T_{\rm eff}(r_{\rm tr})$ (K)	$R_{\rm tr} < R_{\rm cap}$?
	(1)	(2)	(3)	(4)	(5)	(6)	(7)
	2.04×10^{-5} (G1)	0.3	0.80	8.10×10^{4}	209.57	303.72	True
			0.75	6.01×10^{4}	243.18	379.55	True
			0.70	4.37×10^{4}	285.10	481.66	True
	9.07×10^{-7} (G2)	0.3	0.55	2.23×10^{5}	194.56	88.17	False
			0.50	1.43×10^{5}	242.37	122.56	True
			0.45	8.82×10^{4}	308.99	176.37	True

Note. Column (1) is the mass accretion rate $\dot{m}$, Column (2) is the viscosity parameter α, which is fixed to be $\alpha = 0.3$. Column (3) is the magnetic parameter β. Column (4) is the calculated truncation radius of the accretion disk from Equation (6). Column (5) is the corresponding projected velocity in the line of sight at the truncation radius. Column (6) is the corresponding effective temperature at the surface of the accretion disk at the truncation radius.

by combining the emission from the inner ADAF and the outer truncated accretion disk. As for the ADAF, we adopt the self-similar solution for the structure (Narayan & Yi 1994, 1995a, 1995b; Narayan et al. 1995), and the multi-scattering method of the seed photons (including bremsstrahlung, synchrotron radiation of ADAF itself) in the optically thin, hot gas (Coppi & Blandford 1990; Manmoto et al. 1997; Qiao & Liu 2010, 2013). One can refer to Qiao & Liu (2010, 2013) or Manmoto et al. (1997) for the calculation of the emergent spectra of ADAF for details.

In Figure 1, we plot the emergent spectra of the accretion flow with $m = 68$, $\dot{m} = 2.05 \times 10^{-5}$, $\alpha = 0.3$ and $\beta = 0.75$ (hereafter model parameter P1), and $m = 21$, $\dot{m} = 9.32 \times 10^{-7}$, $\alpha = 0.3$ and $\beta = 0.5$ (hereafter model parameter P2), Specifically, in Figure 1, the green solid line is the total emergent spectrum of P1. The green dashed line is the emission from the inner ADAF, and the green dotted line is the emission from the outer truncated accretion disk with truncation radius $R_{\rm tr} = 6.01 \times 10^{4} R_{\rm S}$ calculated from Equation (6). On the other hand, the blue solid line is for the total emergent spectrum of P2. The blue dashed line is the emission from the inner ADAF, and the blue dotted line is the emission from the outer truncated accretion disk with truncation radius $R_{\rm tr} = 1.46 \times 10^{5} R_{\rm S}$ calculated from Equation (6). The two shaded areas denote the UV-optical band (1100 Å–7600 Å) and the X-ray band (0.3–8 keV) respectively, and the black downward arrow represents the upper limit of X-ray luminosity in the band of 0.3–8 keV given by the Chandra X-ray observations.

It can be seen that for model parameter P1, the predicted X-ray luminosity is roughly two orders of magnitude lower than the estimated upper limit of X-ray luminosity, i.e., $L_{\rm X,BH} \approx 2 \times 10^{31}$ erg s^{-1}, which is consistent with observations. For model parameter P2, the case is similar, the predicted X-ray luminosity is roughly four orders of magnitude lower than the upper limit of the X-ray luminosity, also well consistent with observations. The emission of the truncated accretion disk is mainly in the infrared band, which is comparable to the emission of ADAF. However, the emission from both the truncated accretion disk and the ADAF in the infrared is not well constrained by current observations.

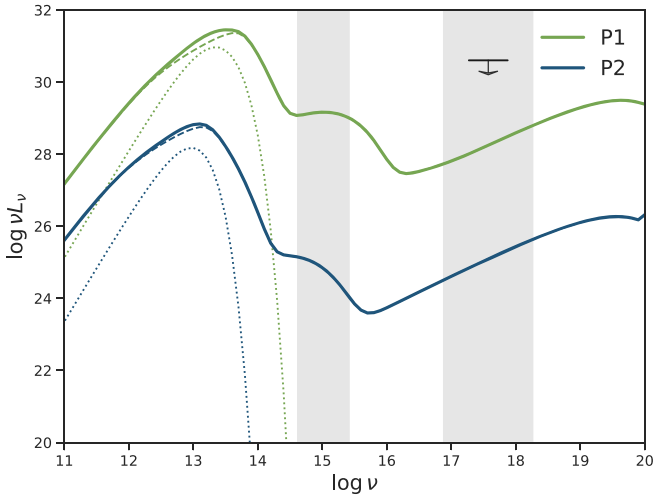

Figure 1. Emergent spectra of the two groups of model parameters (P1: $[m, \dot{m}, \alpha, \beta] = [68, 2.05 \times 10^{-5}, 0.3, 0.75]$; P2: $[m, \dot{m}, \alpha, \beta] = [21, 9.32 \times 10^{-7}, 0.3, 0.50]$.). The green solid line is the total emergent spectra of model parameter P1, and the blue solid line is the total emergent spectra of model parameter P2. The green (blue) dashed line and green (blue) dotted line present the emission of the inner ADAF and the truncated accretion disk for model parameters P1 and P2, respectively. The two shaded areas, from left to right, represent the UV-optical band (1100 Å–7600 Å) and the X-ray band (0.3–8 keV) respectively. The black downward arrow represents the upper limit of the X-ray luminosity of LB-1 given by the Chandra X-ray Observatory.

As we can see from Equation (6), the truncation radius of the accretion disk $r_{\rm tr}$ is very weakly dependent on the value of α. However, the structure and the bolometric luminosity of ADAF are very sensitive to α. In general, the bolometric luminosity of ADAF is proportional to α^{-2} (e.g., Narayan & Yi 1995a; Mahadevan 1997; Qiao & Liu 2009; Li & Qiao 2023). We test the

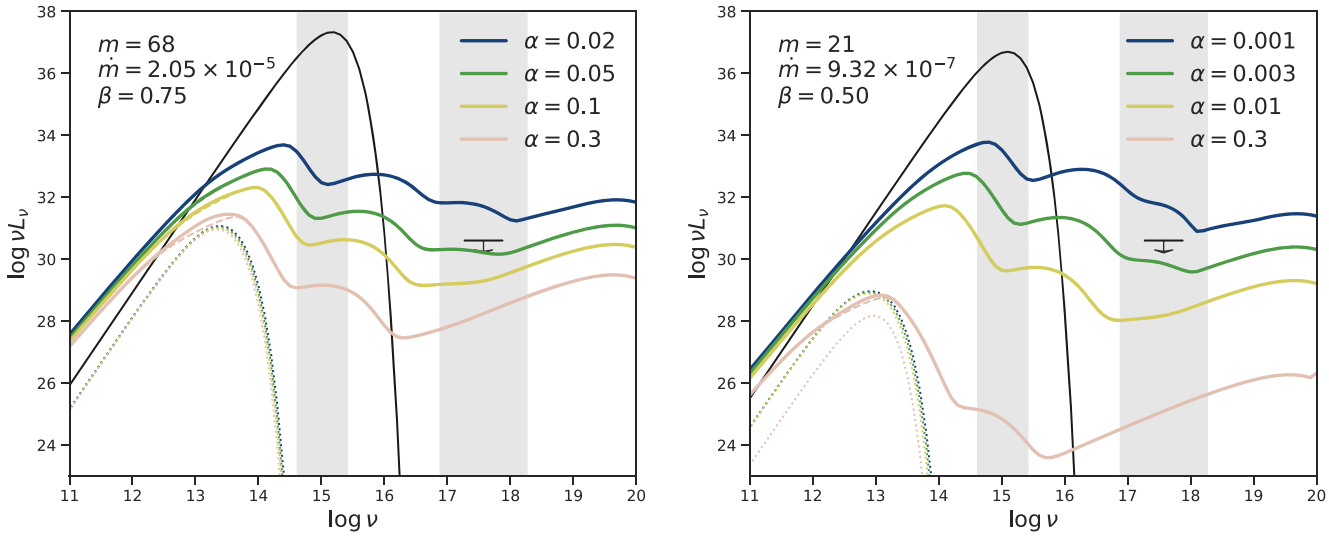

Figure 2. Left panel: Emergent spectra of the model parameter $[m,\ \dot{m},\ \beta] = [68,\ 2.05 \times 10^{-5},\ 0.75]$ for different values of α. From the bottom up, the pink, yellow, green, and blue solid lines are the emergent spectra for $\alpha = 0.3$, 0.1, 0.05 and 0.0,2 respectively. The pink, yellow, green, and blue dotted and dashed lines are the emission from the truncated accretion disk and the emission of the inner ADAF for $\alpha = 0.3$, 0.1, 0.05 and 0.02, respectively. The black solid line denotes the blackbody radiation from the B-type star, with the effective temperature taken to be $T_{\rm eff} = 18{,}000$ K and the radius to be $R_{\rm B} = 9R_{\odot}$. Right panel: Emergent spectra of the model parameter $[m,\ \dot{m},\ \beta] = [21,\ 9.32 \times 10^{-7},\ 0.50]$ for different values of α. From the bottom up, the pink, yellow, green, and blue solid lines are the emergent spectra for $\alpha = 0.3$, 0.01, 0.00,3 and 0.00,1 respectively. The pink, yellow, green, and blue dotted and dashed lines are the emission from the truncated accretion disk and the emission of the inner ADAF for $\alpha = 0.3$, 0.01, 0.003, and 0.001, respectively. The black solid line denotes the blackbody radiation from the B-type star, with the effective temperature taken to be $T_{\rm eff} = 15{,}300$ K and the radius to be $R_{\rm B} = 6R_{\odot}$.

effect of α on the predicted X-ray luminosity. In the left panel of Figure 2, based on the model parameter P1, fixing $m = 68$, $\dot{m} = 2.05 \times 10^{-5}$, and $\beta = 0.75$, we calculate the emergent spectra for different α. From the bottom up, the pink, yellow, green, and blue solid lines are the emergent spectra for $\alpha = 0.3$, 0.1, 0.05, 0.02 respectively. The dotted lines are the emission from the truncated accretion disk with a nearly unchanged truncation radius, i.e., $R_{\rm tr} \approx 6.0 - 5.0 \times 10^4\ R_{\rm S}$ for $\alpha = 0.3$–0.02. The dashed lines are the emission from the inner ADAF. It can be seen that the spectra shift upward systemically with decreasing α. For $\alpha = 0.02$, the X-ray luminosity between 0.3 and 8 keV $L_{\rm X,BH}$ is $\approx 1.5 \times 10^{32}\,{\rm erg\,s^{-1}}$, exceeding the estimated upper limit of X-ray luminosity of $L_{\rm X} \approx 2 \times 10^{31}\,{\rm erg\,s^{-1}}$ given by the Chandra X-ray Observatory. While for $\alpha = 0.05$, the X-ray luminosity $L_{\rm X,BH} \approx 6 \times 10^{30}\,{\rm erg\,s^{-1}}$ is well below the estimated upper limits of the X-ray luminosity. Therefore, α can be roughly constrained to be greater than $\approx$0.05. As a comparison, we plot the emergent spectra of the corresponding B-type star (assuming a single blackbody) based on the system parameter G1, in which the spectrum is calculated as $L_\nu = 4\pi R_{\rm B}^2 \pi B_\nu(T_{\rm eff})$ with $R_{\rm B}$ being the radius and $T_{\rm eff}$ being the effective temperature of the B-type star, denoted as the black solid line. It is clear that the UV-optical band emission is completely dominated by the B-type star, and the emission from the accretion flow in the UV-optical band can completely be neglected, which is consistent with the spectral fitting method adopted for LB-1 in Liu et al. (2019). In the right panel of Figure 2, based on the model parameter P2, fixing $m = 21$, $\dot{m} = 9.32 \times 10^{-7}$ and $\beta = 0.5$, we calculate the emergent spectra for $\alpha = 0.3$, 0.01, 0.003, 0.001, following the same line convention. It can be seen that the spectra shift upward systemically with decreasing α. Specifically, for $\alpha = 0.003$, $L_{\rm X,BH}$ is $\approx 2.4 \times 10^{30}\,{\rm erg\,s^{-1}}$, which is well below the estimated upper limits of the X-ray luminosity. While for $\alpha = 0.001$, $L_{\rm X,BH}$ is $\approx 2.2 \times 10^{32}\,{\rm erg\,s^{-1}}$, exceeding the estimated upper limits of the X-ray luminosity. Therefore, the value of α can roughly be constrained to be greater than $\approx$0.003. The black solid line denotes the spectra of the B-type star, based on the system parameter G2 for $R_{\rm B}$ and $T_{\rm eff}$. Similarly, the UV-optical band emission is also completely dominated by the B-type star. This is consistent with the fitting in Lennon et al. (2021) for the UV-optical spectra, in which the emission from the accretion flow is neglected. One can refer to Table 4 for details on $L_{\rm BH,X}$ and $L_{\rm UV\text{-}Opt,B}/L_{\rm UV\text{-}Opt,BH}$ for different α.

4. Discussion

4.1. On the Viscosity Parameter α and the Magnetic Parameter β

Viscosity is one of the most important physical processes in the BH accretion theory, which controls the angular momentum transport and the heating of the matter in the accretion disk. Shakura & Sunyaev (1973) proposed the so-called α description for the viscosity, in which the value of α is expected to be

Table 4
Luminosities Taking $[m,\ \dot{m},\ \beta] = [68,\ 2.05 \times 10^{-5},\ 0.75]$ and $[m,\ \dot{m},\ \beta] = [21,\ 9.32 \times 10^{-7},\ 0.50]$ Respectively for Different α

	α (1)	$\log L_{\rm bol,BH}$ (erg s^{-1}) (2)	$\log L_{\rm X,BH}$ (erg s^{-1}) (3)	$\log(L_{\rm UV-Opt,B}/L_{\rm UV-Opt,BH})$ (4)	$f(\Delta d;\ \sigma) = \frac{\Delta d}{\sigma^2}\exp\left(-\frac{\Delta d^2}{2\sigma^2}\right),\quad \Delta d \geqslant 0,$ (5)
$m = 68$	0.3	31.77	28.88	8.01	30.11
$\dot{m} = 2.05 \times 10^{-5}$	0.1	32.63	29.93	6.57	31.2
$\beta = 0.75$	0.05	33.23	30.78	5.63	32.01
	0.02	34.04	32.17	4.27	33.19
$m = 21$	0.3	29.11	25.73	11.66	26.87
$\dot{m} = 9.32 \times 10^{-7}$	0.01	32.00	28.80	6.48	30.18
$\beta = 0.50$	0.003	33.07	30.38	4.48	31.75
	0.001	34.12	32.35	3.00	33.34

Note. Column (1) is the adopted α; Column (2) and column (3) are the bolometric luminosity $L_{\rm bol,BH}$ and the X-ray luminosity $L_{\rm X,BH}$ of the accretion flow (inner ADAF + outer truncated accretion disk) for different α; Column (4) is the UV-optical luminosity ratio between the B-type star and the accretion flow around the BH $L_{\rm UV\text{-}Opt,B}/L_{\rm UV\text{-}Opt,BH}$; Column (5) shows the corresponding ionizing luminosities of the inner ADAF for wavelength shorter than 912 Å.

in the range of 0–1. The α-description for the accretion flow has been widely used in different kinds of BH accretion models, such as slim disk for higher mass accretion rates (Abramowicz & Zurek 1981; Abramowicz et al. 1986, 1988; Mineshige et al. 2000; Watarai et al. 2000, 2001; Abramowicz & Fragile 2013), ADAF for lower mass accretion rates (Narayan & Yi 1994, 1995a, 1995b; Narayan et al. 1995, 1998; Manmoto et al. 1997; Qiao & Liu 2013; Balmaverde & Capetti 2014; Nemmen et al. 2014; Yuan & Narayan 2014; Kylafis & Belloni 2015; Fürst et al. 2016), as well as in various hydrodynamical simulations of the accretion flow around BHs (e.g., Sądowski et al. 2015; Sądowski & Narayan 2016; Takahashi et al. 2016; Tang et al. 2017; Jiang et al. 2019). The magnetic parameter β describes the strength of the magnetic field, which can play a role in the structure, dynamics and the radiation of the accretion flow to some extent depending on its magnitude (e.g., Machida et al. 2001; Merloni & Fabian 2001; Liu et al. 2002b, 2003, 2006; Hawley & Krolik 2006; Miller et al. 2006; Tchekhovskoy et al. 2011; McKinney et al. 2012, 2014; Sądowski et al. 2014; Blandford et al. 2019).

As for the study in the present paper, the value of β is constrained by comparing the width of the observed H_α emission line and the predicted truncation radius of the accretion disk from the disk evaporation model. The value of α is constrained by comparing the upper limit of the X-ray luminosity given by the Chandra X-ray Observatory and the theoretical X-ray luminosity of the accretion flow with a structure of an inner ADAF + an outer truncated accretion disk. We discuss the value of β and α, respectively, as follows.

In Section 3.1, based on G1 data, the value of β is constrained to be $\beta \approx 0.75$. Such a value of β is consistent with the basic microphysics in the disk evaporation model, in which the magnetic field in the corona above the accretion disk is believed to be weak, i.e., sub-equipartition ($\beta \gtrsim 0.5$) (Meyer & Meyer-Hofmeister 2002; Qian et al. 2007). Meanwhile, it has been proved that the disk-corona model can very smoothly connect the outer disk-corona and the inner ADAF, which means that the corona above the accretion disk near the truncation radius of the accretion disk shares very similar properties with that of the adjacent ADAF (Liu et al. 1999). ADAF is a kind of radiatively inefficient accretion flow, in which the magnetic field cannot be too strong. Otherwise, if there is a stronger magnetic field, i.e., $\beta < 0.5$, it is very possible that magnetic reconnection can become the dominant mechanism for heating the electrons in the ADAF. This will make ADAF very possibly radiatively efficient, violating the radiatively inefficient nature of the ADAF (Ichimaru 1977; Rees et al. 1982; Narayan & Yi 1994; Manmoto et al. 1997; Narayan & McClintock 2008; Hawley et al. 2011; Qiao et al. 2013; Yuan & Narayan 2014, for review). Based on G2 data, the value of β is constrained to be $\beta \approx 0.5$ (equipartition of the magnetic field), which still can be marginally accepted in the framework of the ADAF model and the disk evaporation model for the essence of a weaker magnetic field.

In Section 3.2, the value of α is constrained to be $\gtrsim$0.05 for taking $m = 68$, $\dot{m} = 2.05 \times 10^{-5}$, and $\beta = 0.75$, and $\gtrsim$0.003 for taking $m = 21$, $\dot{m} = 9.32 \times 10^{-7}$, and $\beta = 0.5$ respectively, which are all roughly consistent with both the numerical simulations (Hawley & Krolik 2001, 2002; Penna et al. 2013; Hogg & Reynolds 2018) and observations of other methods (King et al. 2007; Qiao & Liu 2009, 2018; Martin et al. 2019; Buisson et al. 2021; Chen et al. 2021; Linares et al. 2022). Since in BH binary systems, the X-ray emission is believed to originate from the accretion flow, it is expected that the value of α can be constrained in a narrower range in future X-ray observations of LB-1.

4.2. The Possible Origin of the H_α Line

Liu et al. (2019) reported the presence of a prominent broad H_α emission line that moves in anti-phase compared to stellar absorption lines, which we suggest could originate near the truncation radius between the hot and cool components of the accretion flow. We estimate the luminosity of the H_α line as $L_{H_\alpha} = F_{H_\alpha} \times 4\pi d^2 \approx 10^{33.96}\,\mathrm{erg\,s^{-1}}$, where $F \approx 4.28 \times 10^{-12}\,\mathrm{erg\,s^{-1}\,cm^{-2}}$ is the measured line flux[7] and $d \approx 4.23$ kpc is the distance derived from SED fitting. The inner ADAF and the B-type star are two potential ionizing sources for photoionization. The last column of Table 4 lists the ionizing luminosity of the inner ADAF component for each set of model parameters considered in Section 4.1, calculated as $L_{\rm ion} = \int_{912\text{Å}} L_\nu d\nu$. For those model parameters that satisfy the X-ray non-detection constraint, the resulting ionizing luminosities all fall below the observed H_α luminosity, thereby ruling out photoionization by the inner ADAF as the origin of the H_α emission line. Likewise, we estimate the "maximum" ionizing luminosity from the B-type star that illuminates the accretion disk as $L^{\rm illum}_{\rm ion,B} = L_{\rm ion,B} \times \Omega/4\pi$, where $L_{\rm ion,B}$ is the star's intrinsic ionizing luminosity, calculated from the star SED, and $\Omega = \pi R^2_{\rm cap}/A^2$ is the maximum solid angle subtended by the accretion disk. Using the stellar parameters reported in Liu et al. (2019), Lennon et al. (2021) and their corresponding accretion flow parameters, the maximum ionizing luminosities from the B-type star are $L^{\rm illum}_{\rm ion,B} \approx 10^{33.5}$ and $10^{32.0}\,\mathrm{erg\,s^{-1}}$, respectively. Both values fall below the observed H_α line luminosity, ruling out photoionization by stellar illumination. Additionally, given the high energy required to excite electrons from the ground state to $n = 3$ energy level (as H_α emission arises from the 3 to 2 transition), and the low temperature expected in the thin disk, collisional excitation does not seem to be a viable mechanism either. Therefore, the origin of the observed prominent H_α line remains elusive based on currently available evidence.

4.3. On Other Quiescent Black Holes

A group of binaries containing quiescent BHs have been discovered using radial-velocity and astrometric methods, including AS 386 (Khokhlov et al. 2018), NGC 3201 #12560 and #21859 (Giesers et al. 2018, 2019), VFTS 243 (Shenar et al. 2022), HD 130298 (Mahy et al. 2022), Gaia BH1 and BH2 (Chakrabarti et al. 2023; El-Badry et al. 2023a, 2023b) and BH3 (Gaia Collaboration et al. 2024), MWC 656 (Casares et al. 2014), and 2M05215658 (Thompson et al. 2019). Like LB-1, the natures of MWC 656 and 2M05215658 are also under debate (van den Heuvel & Tauris 2020; Janssens et al. 2023). No X-ray emission was detected for all these sources. The X-ray luminosity upper limits of VFTS 243, Gaia BH1 and BH2, MWC 656 and 2M05215658 were estimated to be 1.45×10^{32}, 3×10^{30}, 8×10^{29}, 10^{32}, 4×10^{31} $\mathrm{erg\,s^{-1}}$ respectively. The wind accretion rates of VFTS 243, Gaia BH1, and BH2 were estimated to be $\approx 2 \times 10^{-11}$, 2×10^{-17}, $3 \times 10^{-14} M_\odot\,\mathrm{yr^{-1}}$, respectively. Such low mass accretion rates would definitely fall into the region of the ADAF solution. Similar to LB-1, it is expected that future X-ray observations can be used to constrain the value of the viscosity parameter α in these binary systems.

[7] Obtained via private communication.

5. Conclusion

In this paper, in the scenario of a B-type main sequence star plus a BH for LB-1, we study the geometry of the accretion flow and calculate the corresponding emergent spectra. Specifically, we first calculate the mass-loss rate of the B-type star and the capture rate by the BH, with which as the initial mass accretion rate, we further calculate the truncation radius of the accretion disk in the framework of disk evaporation model and the corresponding emergent spectra of the accretion flow with an inner ADAF + an outer truncated accretion disk structure. Two groups of data, i.e., G1 (Liu et al. 2019) and G2 (Lennon et al. 2021) are used to test the physics of the accretion flow. We found that both G1 and G2 data can well explain the observed width of the H_α emission line of LB-1 by calculating the truncation radius of the accretion disk with the disk evaporation model with a proper magnetic parameter β. We further constrain the viscosity parameter α by comparing the theoretical X-ray luminosity and the upper limit of the X-ray luminosity given by the Chandra X-ray Observatory. Finally, we discuss the possibility that future X-ray observations for the quiescent BHs could be a good probe for constraining the viscosity of the accretion flow, which can improve our understanding of the microphysics of the accretion flow around a BH.

Acknowledgments

This work was supported by the National Natural Science Foundation of China (grant Nos. 12173048, 12333004, 11988101, and 12273057), and the National Key R&D Program of China (No. 2023YFA1607903). T.S. acknowledges the support from the K.C. Wong Education Foundation.

References

Abdul-Masih, M., Banyard, G., Bodensteiner, J., et al. 2020, Natur, 580, E11
Abramowicz, M. A., Czerny, B., Lasota, J. P., & Szuszkiewicz, E. 1988, ApJ, 332, 646
Abramowicz, M. A., & Fragile, P. C. 2013, LRR, 16, 1
Abramowicz, M. A., Lasota, J. P., & Xu, C. 1986, in IAU Symp. 119, Quasars 119, ed. G. Swarup & V. K. Kapahi (Dordrecht: Reidel), 371
Abramowicz, M. A., & Zurek, W. H. 1981, ApJ, 246, 314
Balmaverde, B., & Capetti, A. 2014, A&A, 563, A119
Blandford, R., Meier, D., & Readhead, A. 2019, ARA&A, 57, 467
Buisson, D. J. K., Fabian, A. C., Gandhi, P., et al. 2021, MNRAS, 500, 3976
Casares, J., Negueruela, I., Ribó, M., et al. 2014, Natur, 505, 378
Chakrabarti, S., Simon, J. D., Craig, P. A., et al. 2023, AJ, 166, 6
Chen, H.-Y., Gu, W.-M., Sun, M., Liu, T., & Yi, T. 2021, ApJ, 921, 147
Coppi, P. S., & Blandford, R. D. 1990, MNRAS, 245, 453
El-Badry, K., & Quataert, E. 2020, MNRAS, 493, L22

El-Badry, K., Rix, H.-W., Cendes, Y., et al. 2023a, MNRAS, 521, 4323
El-Badry, K., Rix, H.-W., Quataert, E., et al. 2023b, MNRAS, 518, 1057
Frank, J., King, A., & Raine, D. J. 2002, Accretion Power in Astrophysics (3rd; Cambridge: Cambridge Univ. Press)
Fürst, F., Müller, C., Madsen, K. K., et al. 2016, ApJ, 819, 150
Gaia Collaboration, Panuzzo, P., Mazeh, T., et al. 2024, A&A, 686, L2
Giesers, B., Dreizler, S., Husser, T.-O., et al. 2018, MNRAS, 475, L15
Giesers, B., Kamann, S., Dreizler, S., et al. 2019, A&A, 632, A3
Hawley, J. F., Guan, X., & Krolik, J. H. 2011, ApJ, 738, 84
Hawley, J. F., & Krolik, J. H. 2001, ApJ, 548, 348
Hawley, J. F., & Krolik, J. H. 2002, ApJ, 566, 164
Hawley, J. F., & Krolik, J. H. 2006, ApJ, 641, 103
Hogg, J. D., & Reynolds, C. S. 2018, ApJ, 854, 6
Ichimaru, S. 1977, ApJ, 214, 840
Irrgang, A., Geier, S., Kreuzer, S., Pelisoli, I., & Heber, U. 2020, A&A, 633, L5
Irrgang, A., Kreuzer, S., & Heber, U. 2018, A&A, 620, A48
Irrgang, A., Przybilla, N., Heber, U., et al. 2014, A&A, 565, A63
Janssens, S., Shenar, T., Degenaar, N., et al. 2023, A&A, 677, L9
Jiang, Y.-F., Stone, J. M., & Davis, S. W. 2019, ApJ, 880, 67
Khokhlov, S. A., Miroshnichenko, A. S., Zharikov, S. V., et al. 2018, ApJ, 856, 158
King, A. R., Pringle, J. E., & Livio, M. 2007, MNRAS, 376, 1740
Kylafis, N. D., & Belloni, T. M. 2015, A&A, 574, A133
Lennon, D. J., Maíz Apellániz, J., Irrgang, A., et al. 2021, A&A, 649, A167
Li, J., & Qiao, E. 2023, MNRAS, 521, 3237
Linares, M., De Marco, B., Wijnands, R., & van der Klis, M. 2022, MNRAS, 512, 5269
Liu, B. F., Mineshige, S., Meyer, F., Meyer-Hofmeister, E., & Kawaguchi, T. 2002a, ApJ, 575, 117
Liu, B. F., Mineshige, S., & Ohsuga, K. 2003, ApJ, 587, 571
Liu, B. F., Mineshige, S., & Ohsuga, K. 2006, AdSpR, 38, 1409
Liu, B. F., Mineshige, S., & Shibata, K. 2002b, ApJL, 572, L173
Liu, B. F., Yuan, W., Meyer, F., Meyer-Hofmeister, E., & Xie, G. Z. 1999, ApJL, 527, L17
Liu, J., Zhang, H., Howard, A. W., et al. 2019, Natur, 575, 618
Liu, J., Zheng, Z., Soria, R., et al. 2020, ApJ, 900, 42
Machida, M., Matsumoto, R., & Mineshige, S. 2001, PASJ, 53, L1
Mahadevan, R. 1997, ApJ, 477, 585
Mahy, L., Sana, H., Shenar, T., et al. 2022, A&A, 664, A159
Manmoto, T., Mineshige, S., & Kusunose, M. 1997, ApJ, 489, 791
Martin, R. G., Nixon, C. J., Pringle, J. E., & Livio, M. 2019, NewA, 70, 7
McKinney, J. C., Tchekhovskoy, A., & Blandford, R. D. 2012, MNRAS, 423, 3083
McKinney, J. C., Tchekhovskoy, A., Sądowski, A., & Narayan, R. 2014, MNRAS, 441, 3177
Merloni, A., & Fabian, A. C. 2001, MNRAS, 321, 549
Meyer, F., Liu, B. F., & Meyer-Hofmeister, E. 2000a, A&A, 354, L67
Meyer, F., Liu, B. F., & Meyer-Hofmeister, E. 2000b, A&A, 361, 175
Meyer, F., & Meyer-Hofmeister, E. 1994, A&A, 288, 175
Meyer, F., & Meyer-Hofmeister, E. 2002, A&A, 392, L5
Miller, J. M., Homan, J., & Miniutti, G. 2006, ApJL, 652, L113
Mineshige, S., Kawaguchi, T., Takeuchi, M., & Hayashida, K. 2000, PASJ, 52, 499
Narayan, R., Mahadevan, R., Grindlay, J. E., Popham, R. G., & Gammie, C. 1998, ApJ, 492, 554
Narayan, R., & McClintock, J. E. 2008, NewAR, 51, 733
Narayan, R., & Yi, I. 1994, ApJL, 428, L13
Narayan, R., & Yi, I. 1995a, ApJ, 444, 231
Narayan, R., & Yi, I. 1995b, ApJ, 452, 710
Narayan, R., Yi, I., & Mahadevan, R. 1995, Natur, 374, 623
Nemmen, R. S., Storchi-Bergmann, T., & Eracleous, M. 2014, MNRAS, 438, 2804
Penna, R. F., Sądowski, A., Kulkarni, A. K., & Narayan, R. 2013, MNRAS, 428, 2255
Qian, L., Liu, B. F., & Wu, X.-B. 2007, ApJ, 668, 1145
Qiao, E., & Liu, B. F. 2009, PASJ, 61, 403
Qiao, E., & Liu, B. F. 2010, PASJ, 62, 661
Qiao, E., & Liu, B. F. 2013, ApJ, 764, 2
Qiao, E., & Liu, B. F. 2018, MNRAS, 477, 210
Qiao, E., Liu, B. F., Panessa, F., & Liu, J. Y. 2013, ApJ, 777, 102
Raskin, G., van Winckel, H., Hensberge, H., et al. 2011, A&A, 526, A69
Rees, M. J., Begelman, M. C., Blandford, R. D., & Phinney, E. S. 1982, Natur, 295, 17
Shakura, N. I., & Sunyaev, R. A. 1973, A&A, 24, 337
Shenar, T., Bodensteiner, J., Abdul-Masih, M., et al. 2020, A&A, 639, L6
Shenar, T., Sana, H., Mahy, L., et al. 2022, NatAs, 6, 1085
Simón-Díaz, S., Maíz Apellániz, J., Lennon, D. J., et al. 2020, A&A, 634, L7
Sądowski, A., & Narayan, R. 2016, MNRAS, 456, 3929
Sądowski, A., Narayan, R., McKinney, J. C., & Tchekhovskoy, A. 2014, MNRAS, 439, 503
Sądowski, A., Narayan, R., Tchekhovskoy, A., et al. 2015, MNRAS, 447, 49
Taam, R. E., Liu, B. F., Yuan, W., & Qiao, E. 2012, ApJ, 759, 65
Takahashi, H. R., Ohsuga, K., Kawashima, T., & Sekiguchi, Y. 2016, ApJ, 826, 23
Tang, Y., MacFadyen, A., & Haiman, Z. 2017, MNRAS, 469, 4258
Tchekhovskoy, A., Narayan, R., & McKinney, J. C. 2011, MNRAS, 418, L79
Thompson, T. A., Kochanek, C. S., Stanek, K. Z., et al. 2019, Sci, 366, 637
Tkachenko, A. 2015, A&A, 581, A129
van den Heuvel, E. P. J., & Tauris, T. M. 2020, Sci, 368, eaba3282
Vink, J. S., de Koter, A., & Lamers, H. J. G. L. M. 2000, A&A, 362, 295
Watarai, K.-y., Fukue, J., Takeuchi, M., & Mineshige, S. 2000, PASJ, 52, 133
Watarai, K.-y., Mizuno, T., & Mineshige, S. 2001, ApJL, 549, L77
Yuan, F., Cui, W., & Narayan, R. 2005, ApJ, 620, 905
Yuan, F., & Narayan, R. 2014, ARA&A, 52, 529
Yungelson, L. R., Kuranov, A. G., Postnov, K. A., & Kolesnikov, D. A. 2020, MNRAS, 496, L6
Zhang, H., Yuan, F., & Chaty, S. 2010, ApJ, 717, 929